

Large-Area Heteroepitaxial Nanostructuring of Molecular Semiconductor Films for Enhanced Optoelectronic Response in Flexible Electronics

Kwang-Won Park, Raaghesh Vijayan, and Trisha L. Andrew*

Organized nano- and microstructures of molecular semiconductors display interesting optical and photonic properties, and enhanced charge carrier mobilities, as compared to disordered thin films. However, known directed-growth and self-organization strategies cannot create structured molecular heterojunctions and cannot be practically incorporated into existing device fabrication routines to create large-area optoelectronic devices. Here, an ultrathin (<2 nm) seed layer of the compound coronene creates 1D nanostructures of an electron-transporting molecule (IFD) is shown, which possesses an intrinsic proclivity to form disordered thin films in the absence of the seed layer. It is revealed that nanostructured IFD films exhibit enhanced light absorption and emission, and greater electron mobilities, as compared to amorphous counterparts. This seed layer strategy creates uniform IFD nanowires over large areas of up to 18 mm² at low processing temperatures. Notably, the coronene seed layer creates IFD nanowires when applied over either oxide surfaces or predeposited organic layers, meaning that this structuring approach can be integrated into diode manufacturing routines to realize large-area flexible optoelectronic devices. Flexible organic light-emitting diodes and fullerene-free organic solar cells containing IFD nanowires in the photoactive layer to demonstrate that molecular nanostructures can lead to robust, large-area device arrays on flexible substrates being fabricated.

1. Introduction

Organized nano- and microstructures of molecular semiconductors are known to display interesting optical and photonic properties, and enhanced charge carrier mobilities, as compared to amorphous or polycrystalline thin films.^[1] Incorporating these organized structures into molecular heterojunctions promises access to next-generation flexible optoelectronics with enhanced

performances. However, it is particularly difficult to direct growth and/or induce self-organization in films of molecular semiconductors with octahedral geometries, such as most organometallic emitters and phosphors, and steric constraints, such as twisted core conformations or bulky substituents.^[2] Moreover, common directed-growth and self-organization strategies that induce order in single-component thin films, such as those involving elevated processing temperatures^[1b,3] and self-assembled monolayers (SAMs),^[4] often fail when applied to molecular heterojunctions. Either only one layer in the heterojunction will be ordered while the other remains amorphous, or the growth/self-assembly method leads to suboptimal intermolecular configurations at the heterojunction.


Templating layers and external scaffolds have created large-area nanostructured heterojunction arrays,^[5] but cannot be readily integrated into device manufacturing routines as these layers and scaffolds need to be removed, often using harsh or damaging wet chemical procedures.

Kinetically-controlled physical vapor transport (PVT) has produced exquisite one-dimensional molecular heterojunctions with optimal intermolecular ordering at the organic-organic junction,^[6] but such structures are formed haphazardly and cannot be reliably and uniformly created over large areas on a variety of substrates, particularly flexible plastic surfaces. Furthermore, PVT utilizes the intrinsic crystallization proclivity of a molecular semiconductor, meaning that molecules with twisted or rotatable substituents and molecules that resist crystallization, even above their T_g ^[7] will not form ordered heterojunctions during PVT.

Here, we present an unprecedented approach using an ultrathin (<2 nm) nucleation layer of the compound coronene to create crystalline nanostructures of an electron-transporting molecular semiconductor that is observed to have an intrinsic proclivity to form disordered films, indenofluorenedione (IFD). The current work is distinguished from previous efforts in directed growth and self-organization of molecular semiconductors by a number of promising features, which include: the low-temperatures needed for the process; the absence of vacuum breaks between steps; large-area, uniform formation

K.-W. Park, R. Vijayan, T. L. Andrew
Department of Chemistry
University of Massachusetts Amherst
Amherst, MA 01003, USA
E-mail: tandrew@umass.edu

T. L. Andrew
Department of Chemical Engineering
University of Massachusetts Amherst
Amherst, MA 01003, USA

 The ORCID identification number(s) for the author(s) of this article can be found under <https://doi.org/10.1002/adfm.202113085>.

DOI: 10.1002/adfm.202113085

of nanowires over seeded areas; the ability to pattern nanowire-containing areas using shadow-masking; and the enhancement of both electrical and photophysical properties in nanostructures formed with molecules containing bulky, freely-rotating substituents. Nanoscale ordering in the active layer often results in quenched emission efficiencies^[8] and, therefore, in an optoelectronic device, there is a need to have separated charge transport and emissive layers. However, an interesting outcome of our work is the observation of increased solid-state luminescence efficiency in IFD nanowires, concomitant with improved charge transport, upon ordering—nanostructured IFD films exhibit several orders of magnitude higher electron mobility and four-times stronger fluorescence quantum yield, as compared to amorphous counterparts. Notably, the coronene seed layer creates IFD nanowires when applied over either common oxide surfaces or other predeposited organic layers, meaning that the seed layer approach reported herein can be readily adapted into existing diode manufacturing routines to create a uniform crystalline nanostructure over large areas. We fabricate both organic light-emitting diodes (OLEDs) and fullerene-free organic solar cells (OSCs) containing IFD nanowires as an electron-transporting photoactive layer to demonstrate that molecular nanostructures can lead to robust, large-area device arrays on flexible substrates.

2. Results and Discussion

2.1. Molecular Properties

We speculated that coronene can provide an excellent platform as a nucleation center for the crystallization of small molecules due to strong intermolecular interactions. Its unique planar and pi-electron rich molecular structure enables efficient charge-transfer complexes in a solid state.^[9] In addition, vapor deposited coronene films tend to form vertical nanowires because intermolecular interaction is much stronger than the interactions between molecules and a surface.^[10] To investigate whether strong interaction between coronene and molecular semiconductors with bulky rotatable substituents can induce ordering, we investigated 5,11-diphenylindeno[1,2-*b*]fluorene-6,12-dione (Dp-IFD) because aromatic ketones are known to be competitive electron accepting materials.^[11]

Figure 1a shows the chemical structure of Dp-IFD that consists of indeno[1,2-*b*]fluorene-6,12-dione (IFD) moiety and phenyl substituents on the 5- and 11- position of the IFD framework. The geometry-optimized structure of Dp-IFD is shown in Figure 1b, obtained by density functional theory (DFT) calculations under B3LYP functional with 6–311G(2d, p) basis set. The molecular structure displayed along the y-axis shows that the IFD framework has planar geometry and a fully conjugated system throughout the molecule. Recently, IFD derivatives have been of interest due to their rigid and planar structure, high electron affinity, and charge transport abilities.^[12] Since the electron-withdrawing carbonyl groups lower the lowest unoccupied molecular orbital (LUMO) level, IFD derivatives were reported to show n-type field-effect transistor (FET) properties. In addition, the planar structure of IFD derivatives facilitates dense packing in crystals owing to the strong π - π interactions with the

interplanar distances between 3.22 Å and 3.45 Å^[12a–d]. Thanks to the high crystallinities, IFD-based FETs yield high electron mobilities. For example, fluorine substituted IFD exhibited a field-effect mobility of 0.16 cm² V⁻¹ S⁻¹.^[12c] More recently, Zhang et al. reported that butylthio-modified IFD exhibited higher electron mobilities up to 0.65 cm² V⁻¹ S⁻¹.^[12e]

Despite these interesting electronic properties of IFD derivatives, optoelectronic properties of Dp-IFD have been uninvestigated to date. This is attributed to the fact that phenyl substituents have nothing to do with tuning the electronic properties of the molecule, and they are largely distorted (e.g., dihedral angle $\varphi \approx 90^\circ$) to minimize interactions between nearby C-H bonds and the IFD framework. It is known that twisted phenyl substituents prevent close intermolecular packing, and thus lead to disordered aggregates.^[13] Accordingly, Dp-IFD barely crystallize even at elevated temperatures up to 300 °C (Figure S1, Supporting Information), and this inherent propensity to form disordered thin films makes Dp-IFD less attractive. Rather, an increased solid-state luminescence efficiency with improved charge transport is the result of the seed-induced nanostructuring, which will be discussed.

2.2. Morphological Characterization of Films

The surface morphology of Dp-IFD thin films was examined, which were fabricated by physical vapor deposition (PVD). The fabrication process is described in Figure 1c. As opposed to the pristine films of Dp-IFD, when an ultra-thin layer (ca. < 2 nm) of coronene is applied as a nucleation seed layer, subsequent Dp-IFD thin-films can form crystalline nanostructures. We highlight this facile method to fabricate crystalline molecular semiconductor thin films at low temperatures and in the absence of vacuum breaks between steps.

Figure 1d shows the SEM image of Dp-IFD thin film on Si substrate grown by PVD. We observed that as-deposited film has a very uniform, smooth, and featureless surface. From the AFM image shown in Figure 1e, amorphous islands were observed, indicating that the pristine Dp-IFD films hardly crystallize and remain disordered. Although we manipulated growth kinetics to obtain kinetically trapped features by changing extrinsic parameters, including deposition rate and substrate temperature,^[13] Dp-IFD thin films intrinsically prefer a disordered state. The twisted phenyl substituents of the molecule are likely responsible for its amorphous nature. On the other hand, we discovered that Dp-IFD can form crystalline nanostructures when deposited on an ultra-thin film of coronene as a nucleation seed layer. The crystalline features can be seen in the SEM image (Figure 1e) and the corresponding AFM image (Figure 1g). We found that some of the crystalline nanostructures grow up to 150 nm even if the same amount of Dp-IFD molecules were deposited as a 20-nm-thick pristine film without a seed layer (Figure S2, Supporting Information). This suggests that strong intermolecular interactions between coronene and Dp-IFD induce nanoscale ordering. When Dp-IFD molecules reach a surface during the PVD process, they have some kinetic energy of diffusion (K_{sur}) on the surface before they nucleate.^[13] These molecules are no longer mobile when they meet coronene seed layer, due to the strong non-covalent

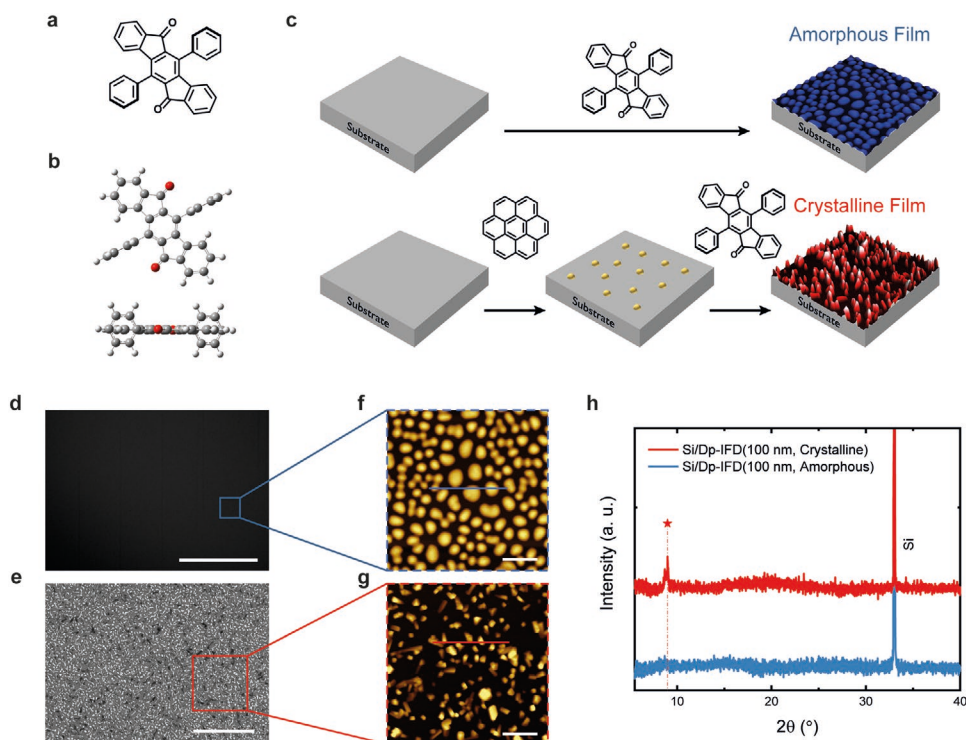


Figure 1. Molecular structure of Dp-IFD, morphological and crystallinity characterization of films. a) Chemical structure of Dp-IFD. b) Optimized molecular structures of Dp-IFD obtained by DFT calculations under B3LYP/6-311+G(2d, p). c) Schematic illustration of the fabrication process of amorphous (top) and crystalline (bottom) Dp-IFD thin-films. d, e) SEM images and f, g) AFM topographic images of amorphous (d, f) and crystalline (e, g) Dp-IFD thin films on Si substrates, respectively. Samples were prepared with a deposition rate of 0.3 \AA s^{-1} at RT and a thickness of 20 nm. Scale bars are 40, 5, 1, and 1 μm for (d), (e), (f), (g), respectively. h) XRD patterns of 100-nm-thick amorphous (blue) and crystalline (red) Dp-IFD thin films on Si substrates.

attraction between coronene and Dp-IFD molecules. Subsequently, more and more molecules coalesce to form crystalline nanostructures, often referred to as the “seed-induced crystallization” method.^[4b,14]

Moreover, as displayed in Figure 1h, the XRD pattern of the film with a coronene seed layer shows a diffraction peak at $2\theta = 8.98^\circ$, while the film without a coronene seed layer has no XRD peak, indicating that a coronene seed layer causes the crystallization of Dp-IFD molecules in the film. In order to gain more insight into the intermolecular organizations of the films, grazing-incident wide-angle X-ray scattering (GIWAXS) was conducted (Figure S3, Supporting Information). In addition to the GIWAXS images, intensity integrals along the radial axis from 0° to 90° is plotted for all the GIWAXS patterns as shown in Figure S3e, Supporting Information. The diffraction pattern of amorphous Dp-IFD did not have any distinct peaks and the obtained pattern was identical to that of the control ITO substrate (Figure S3a, Supporting Information). This indicates that the pristine Dp-IFD film is disordered lacking long-range order. Interestingly, however, 20-nm-thick neat film of coronene shows a sharp ring with a stronger intensity along the vertical axis, which is evidence for the preferred orientation of coronene molecules along the normal to the substrate (Figure S3b, Supporting Information). The ring located at $q = 0.652 \text{ \AA}^{-1}$ is attributed to the (001) plane of coronene crystals with the d -spacing of 9.63 \AA .^[15] This is consistent with the thin film XRD pattern, which exhibits a diffraction peak at $2\theta = 9.45^\circ$ (Figure S4,

Supporting Information). The ring located at $q = 1.789 \text{ \AA}^{-1}$ is also attributable to the π - π interaction with the intermolecular distance of 3.53 \AA . The diffraction patterns observed in Figure S4d, Supporting Information, reveal that Dp-IFD film grown on the coronene seed layer is crystalline. The arc-shaped scattering intensity corresponds to the d -spacing of 9.84 \AA implies that Dp-IFD molecules are tilted approximately 48° on the surface, and prefer out-of-plane orientation. In addition, it should be noted that this seed-induced crystallization method can be generalized to different substrates, including Si, ITO, and glass, which is beneficial for versatile device applications (Figure S5, Supporting Information).

Significantly, our strategy is totally distinguished from the aforementioned methods for directed growth and self-organization of molecular semiconductors because the presence of coronene in the crystalline Dp-IFD thin films is negligible. A small amount of coronene can provide an excellent platform as a nucleation center due to strong intermolecular interactions. The AFM image of 1-nm-thick coronene thin film shows that tiny molecular seed islands are well-dispersed (Figure S6, Supporting Information), which implies that coronene molecules nucleates first rather than makes monolayer on the substrate. Additionally, ultrathin layer of coronene is barely observable even with an electron microscope. Since the amount of coronene molecules is insignificant relative to the Dp-IFD thin film, and coronene does not cover the entire surface, presumably the coronene seed layer does not influence

the optoelectronic properties of Dp-IFD. Ultraviolet photoelectron spectroscopy (UPS) spectra (Figure S7a, Supporting Information) shows that the density of states of amorphous and crystalline Dp-IFD thin films are almost identical with the highest occupied molecular orbital (HOMO) level of 6.5 eV, and there was no characteristic signal from coronene molecules. As UPS is the most sensitive method to characterize molecular thin films, we further confirm that the effect of the coronene seed layer underneath the crystalline Dp-IFD thin film is negligible with respect to optical as well as electronic interferences.

2.3. Heterojunction Formation of Heteroepitaxial Nanostructures

For the integration into optoelectronic devices, it is imperative that the coronene seed layer is capable of creating crystalline nanostructures in heterojunctions. Based on the HOMO level of Dp-IFD of 6.5 eV, we estimated the LUMO level of 4.26 eV using an optical band gap ($E_{opt} = 2.24$ eV). In comparison with some notable hole and electron transporting molecular semiconductors (Figure S7b, Supporting Information), the band energy levels of Dp-IFD thin film are closer to the electron transporting materials, such as C_{60} ^[16] and 3,4,9,10-perylene-tetracarboxylic dianhydride (PTCDA).^[17] Therefore, we posit that Dp-IFD thin films should act as an electron-transporting material in an active layer with other molecular semiconductors. The energy diagram shows that Indium(III) phthalocyanine chloride (InClPc) makes a type II heterojunction with Dp-IFD (Figure 2a). In addition, InClPc and Dp-IFD have a complementary light absorption (Figure 2b), which is beneficial for OSC applications with enhanced light harvesting ability.

Surface morphology of InClPc/Dp-IFD heterojunctions was examined by AFM to investigate whether the crystalline nanostructures can be observed at the organic-organic junction using the seed-induced method (Figure 2c–f). First, InClPc film is very smooth and featureless (Figure 2d) with an RMS roughness of 3.40 nm. Likewise, the surface morphology of Dp-IFD film on InClPc is also similarly smooth (Figure 2e), as the surface roughness remains low as 0.79 nm. However, after the coronene seed layer is applied on top of InClPc film, crystalline nanostructures of Dp-IFD are observed (Figure 2f). The surface roughness increases drastically up to 81.74 nm due to the large crystalline nanostructures. It is noteworthy that the seed-induced nanostructuring strategy is universally amenable to any surface, including common oxides and organic layers, suggesting that our approach herein can be readily integrated into existing diode manufacturing routines to realize large-area flexible optoelectronic devices.

2.4. Charge Transport Properties

We explored the electron-transporting properties of Dp-IFD thin films by making electron-only devices with a configuration of ITO/TiO₂ (35 nm)/Dp-IFD (200 nm)/Ca (15 nm)/Al (80 nm) (Figure 3a). As shown in Figure 3b, space charge limited currents (SCLC) were measured for both amorphous and crystalline Dp-IFD thin films. We observed that the amorphous device exhibits poor electron mobilities of $3.91 \times 10^{-8} \text{ cm}^2 \text{ V}^{-1} \text{ s}^{-1}$, whereas the crystalline device yields 4-orders of magnitude higher mobilities of $2.85 \times 10^{-4} \text{ cm}^2 \text{ V}^{-1} \text{ s}^{-1}$, based on the Mott-Gurney law to fit the I - V curves. This significantly higher mobility reveals that the seed-induced crystallization strategy is conducive for the improved charge transport

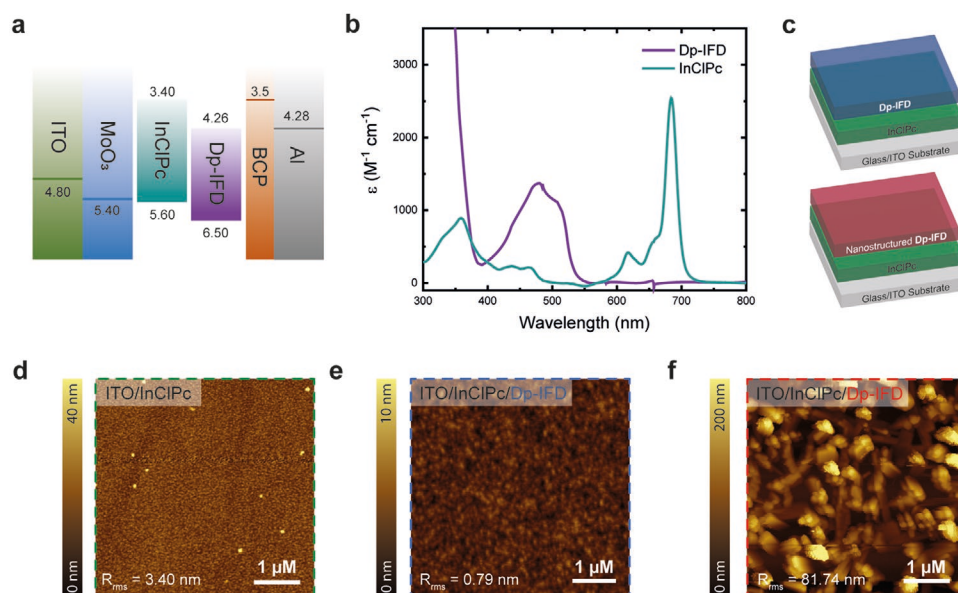


Figure 2. Heterojunction formation of heteroepitaxial nanostructures. a) Energy diagram of the OSC device configuration with InClPc and Dp-IFD comprising heterojunction. b) UV-Vis absorption spectra of Dp-IFD (purple) and InClPc (green). c) Film architectures of amorphous and crystalline Dp-IFD films in the heterojunction with InClPc for the AFM measurements in Figure 2d–f. d–f) AFM images of InClPc on ITO substrate (d), amorphous Dp-IFD on InClPc (e), and crystalline Dp-IFD on InClPc (f). All films are 40-nm-thick.

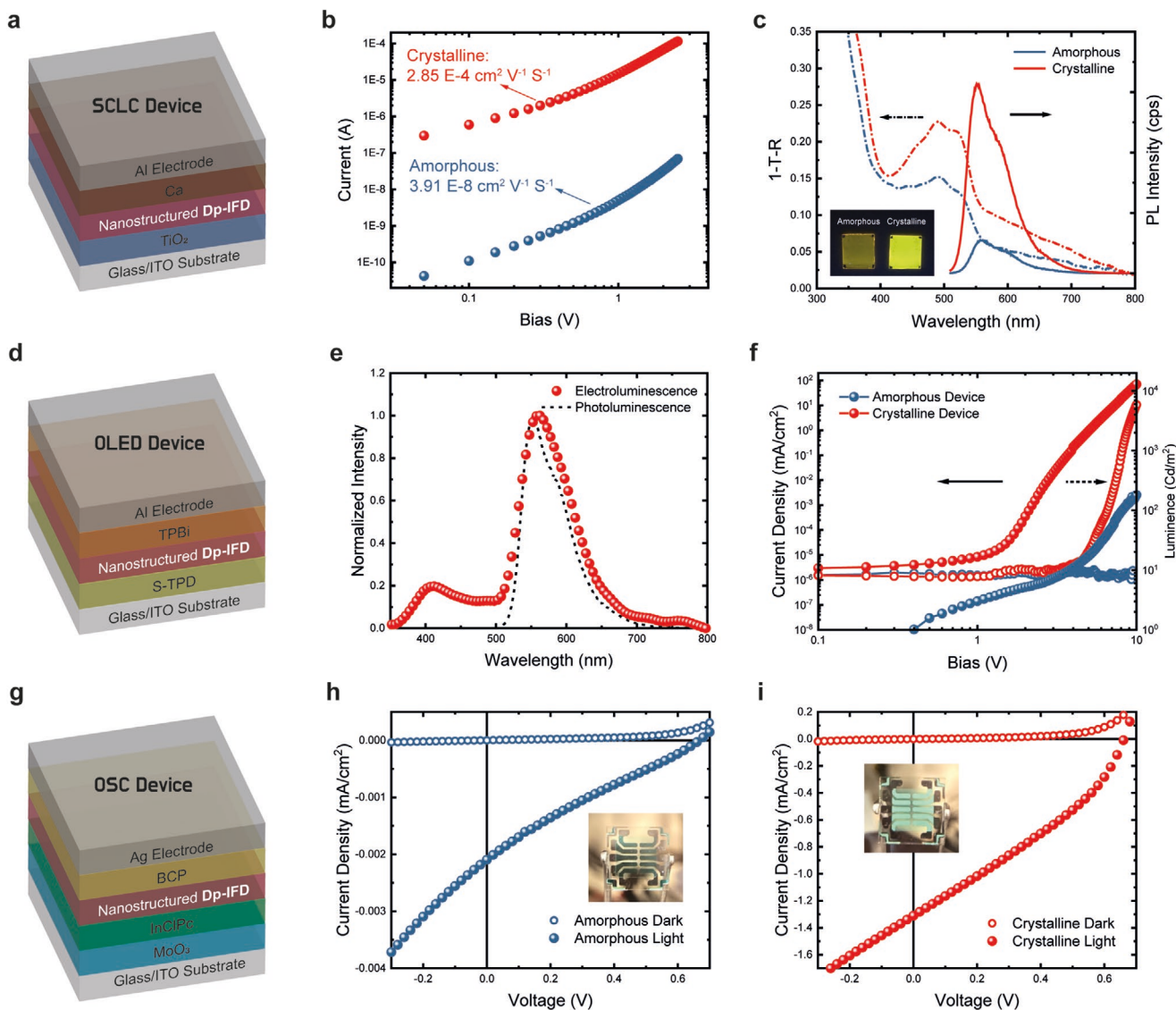


Figure 3. Optoelectronic properties and device performances using Dp-IFD thin films. a) Schematic of SCLC device architecture. b) I - V curves of SCLC devices with the amorphous (blue) and crystalline (red) Dp-IFD thin films. c) UV-vis absorption (left) and PL (right) spectra of amorphous (blue) and crystalline (red) Dp-IFD thin films on glass substrates. d) Schematic of OLED device architecture. e) PL (black dash) and EL (red circle) spectra of the crystalline film and the OLED device with the crystalline film, respectively. f) Current density (left, solid circles) and luminance (right, hollow circles) curves as a function of bias voltage of non-doped OLED devices with the amorphous (blue) and crystalline (red) Dp-IFD films. g) Schematic of OSC device architecture. h,i) Current density-voltage curves of OSC devices with amorphous (h) and crystalline (i) films. Inset pictures are corresponding devices.

properties of Dp-IFD films. In addition, we performed conductive atomic force microscopy (c-AFM) on the same samples using Pt/Ir coated cantilever as a top electrode for comparison (Figure S8, Supporting Information). Interestingly, SCLC data of the amorphous sample give an average electron mobility of $5.54 \times 10^{-4} \text{ cm}^2 \text{ V}^{-1} \text{ s}^{-1}$, which is in good agreement with that of the device. On the contrary, SCLC of the crystalline sample obtained by c-AFM shows a mobility of $1.73 \times 10^{-2} \text{ cm}^2 \text{ V}^{-1} \text{ s}^{-1}$, which is two-orders of magnitude higher than that of the device. We speculated that the smaller SCLC mobility of the bulk device is attributed not only to the grain boundaries between crystalline regions in 200-nm-thick film, but to the irregular thickness of the film originating from the innate properties of nanocrystalline structures.

2.5. Optical Properties

Figure 3c shows UV-vis absorption and photoluminescence (PL) spectra of Dp-IFD thin films. We found that the absorption features observed in the solution phase^[12b,d] are preserved in the solid state. It can be seen that the crystalline film exhibited higher absorption in the region between 400 nm and 600 nm, than that of amorphous film. This is attributable to the lower reflectivity of the crystalline Dp-IFD film, originating from the crystalline nanostructures on the surface. Under the excitation at $\lambda_{\text{ex}} = 490 \text{ nm}$, prominent PL emission peaks were observed at $\lambda_{\text{em}} = 550 \text{ nm}$ for the crystalline sample and $\lambda_{\text{em}} = 560 \text{ nm}$ for the amorphous counterpart. Surprisingly, we observed that the PL intensities of the crystalline thin film were greatly higher

than that of the amorphous sample, yielding fluorescence quantum yield (ϕ_f) of 21.2% and 4.89% for crystalline and amorphous thin films, respectively. This is a four-fold increase, and the inset picture of Figure 3c clearly manifests that crystalline Dp-IFD thin film yields a much brighter yellow light emission under UV excitation ($\lambda = 365$ nm). This phenomenon can be explained by the aggregation-induced emission (AIE) effect,^[18] exhibiting efficient emission properties through the promotion of radiative pathways as intramolecular motion is restrained in the aggregated state, which may induce non-radiative pathways. Dp-IFD molecule has easily rotatable phenyl substituents, and the rotations of phenyl rings could facilitate the non-radiative decay of its excited state. Therefore, in solution, this intramolecular rotation makes the molecule non-emissive. In contrast, restriction of the intramolecular rotation in the solid-state prevents the non-radiative decay, thus making the molecule emissive. The less reorganization energy of the crystalline sample relative to that of the amorphous sample further validates that the molecular motion is more restricted in the crystalline film. This led us to fabricate OLED devices with Dp-IFD thin films to take advantage of unique solid state emission properties, and the results are discussed in the next section.

2.6. OLED Performance

In most previously reported OLEDs, luminescent molecules are employed in a host material to avoid the aggregation-caused quenching (ACQ) effect. To optimize the device performance, it is inevitable to control the doping concentration.^[19] Due to the host-guest system, the emission and charge transport properties are compromised. However, Dp-IFD is free from the ACQ effects of light emission, and thus requires no dopant for OLED device fabrication. In this regard, non-doped OLEDs were fabricated through PVD technique with a device configuration of ITO/*N,N'*-Bis(3-methylphenyl)-*N,N'*-bis(phenyl)-2,7-diamino-9,9-spirobifluorene (*s*-TPD)/Dp-IFD/1,3,5-Tris(1-phenyl-1Hbenzimidazol-2-yl)benzene (TPBi)/Al (Figure 3d). In this device, *s*-TPD and TPBi function as a hole transporting (HTL) and an electron transporting layer (ETL), respectively. Figure 3f shows that the device with amorphous Dp-IFD displays no light emitting properties. In contrast, it can be seen that the device with the crystalline emitting layer has a very low turn-on voltage of 1.5 V and emits bright yellow light with a maximum luminance of 5900 cd m⁻². In consequence, the device yields maximum current efficiency and power efficiency of 8.35 cd A⁻¹ and 2.64 lm W⁻¹, respectively. The EL spectrum of the device is largely coincident with the PL spectrum of the thin film, indicating that the EL mainly originates from the crystalline Dp-IFD emitting layer (Figure 3e). It should be noted that nanostructured Dp-IFD can play roles in charge transportation as well as emissions in an OLED device operation. Furthermore, the device efficiency and brightness are comparable to other yellow emitting OLEDs.^[20]

2.7. Organic Solar Cell (OSC) Performance

Besides the interesting charge transport and emission properties, Dp-IFD has a good light absorption ability with a broad

Table 1. The OSC devices performance of amorphous and crystalline Dp-IFD active layers.

| Devices | V _{oc} [V] | J _{sc} [mA cm ⁻²] | FF | Eff (%) |
|-------------|---------------------|--|--------------|------------------|
| Amorphous | 0.59 ± 0.06 | 0.003 ± 0.0007 | 0.24 ± 0.01 | 0.0004 ± 0.00001 |
| Crystalline | 0.67 ± 0.01 | 1.31 ± 0.02 | 0.33 ± 0.003 | 0.28 ± 0.005 |

visible light range up to 550 nm (Figure 3c). In conjunction with the n-type characteristics, we postulated that Dp-IFD can act as a good acceptor in the active layer of OSC devices. To test our hypothesis, the OSC devices were explored with a device configuration of ITO/MoO₃/InClPc/Dp-IFD/2,9-Dimethyl-4,7-diphenyl-1,10-phenanthroline (BCP)/Al (Figure 3g). In this configuration, InClPc and Dp-IFD function as a p- and n-type heterojunction, respectively. Figure 3h,i show the current density-voltage characteristics of the devices using amorphous and crystalline Dp-IFD thin films, respectively, under 1 sun AM 1.5G illumination, and the device performances are summarized in Table 1. It is interesting to note that an OSC device with an amorphous acceptor layer shows very poor photovoltaic properties with an efficiency of as low as 0.0004%. This low efficiency value is ascribed to the poor current densities of the device, which indicates that amorphous film generates very little photocurrents. On the other hand, the crystalline device exhibits a significantly higher efficiency of 0.28% with a current density of 1.31 mA cm⁻². This 700-times higher efficiency of the crystalline Dp-IFD devices when compared to amorphous devices can be explained by two factors. First, the photocurrent difference is consistent with the difference between charge transport properties of amorphous and crystalline films as characterized with SCLC measurements (Figure 3b). The amorphous film is a poor electron transporter, whereas the crystalline film exhibited four orders of magnitude higher electron mobility. Thus, it can be hypothesized that even photo-induced excitons are generated in the amorphous Dp-IFD active layer, they could not reach the active layer interface due to the lack of ordering. Consequently, the PL quenching experiment shows that amorphous Dp-IFD thin film exhibits an exciton diffusion length of 8.91 nm (Figure S9, Supporting Information). This short exciton diffusion length might be one of the reasons for the lower photocurrent of the amorphous devices. Second, the nanostructures of the active layer also play a vital role in the light absorption process in OSCs. One can see that the amorphous OSC device is transparent, while the crystalline device is opaque, as shown in the insets of Figure 3h,i, respectively. As discussed earlier, the rough surface of the crystalline film makes it less reflective (Figure 3c), and thereby the crystalline film could absorb more light into the film. Additionally, the nanostructures can act as optical waveguides, trapping incident light in the active layer.^[21]

On one hand, the implementation of light trapping in OSC is promising for light absorption. However, on the other hand, these nanostructures can hinder the efficient charge collection of the device. As discussed earlier, the surface roughness of crystalline Dp-IFD in heterojunction with InClPc is considerable (Figure 2f), compared with the amorphous counterpart. We observed that the nanostructures still remain after deposit upper layers, such as BCP and TPBi layers of the OSC and OLED devices, respectively (Figure S10, Supporting Information). This high rough surface could generate electrical

pinholes in the OSC devices, leading to a decrease in the device shunt resistance (R_{sh}). Consequently, the crystalline device shows a relatively low R_{sh} of $6.9 \times 10^2 \Omega \text{ cm}^2$ compared with the amorphous device (R_{sh} of $2.3 \times 10^5 \Omega \text{ cm}^2$). This low R_{sh} value is responsible for the low fill factor of the device, leading to reduced efficiency. Nonetheless, it should be noted that the transformation of Dp-IFD from amorphous to crystalline active layer through the seed-induced crystallization strategy could notably improve the device efficiency.

2.8. Large-Area Flexible Devices

Interestingly, the coronene seed layer can be patterned via shadow-masking to selectively direct the formation of Dp-IFD nanostructures in desired areas. Obviously, pristine Dp-IFD film without the underneath seed layer remains amorphous, while the film grown on the seeded region creates crystalline nanostructures (Figure 4a,b). SEM images show that the seeded region is clearly distinguishable from the pristine film grown on the unseeded

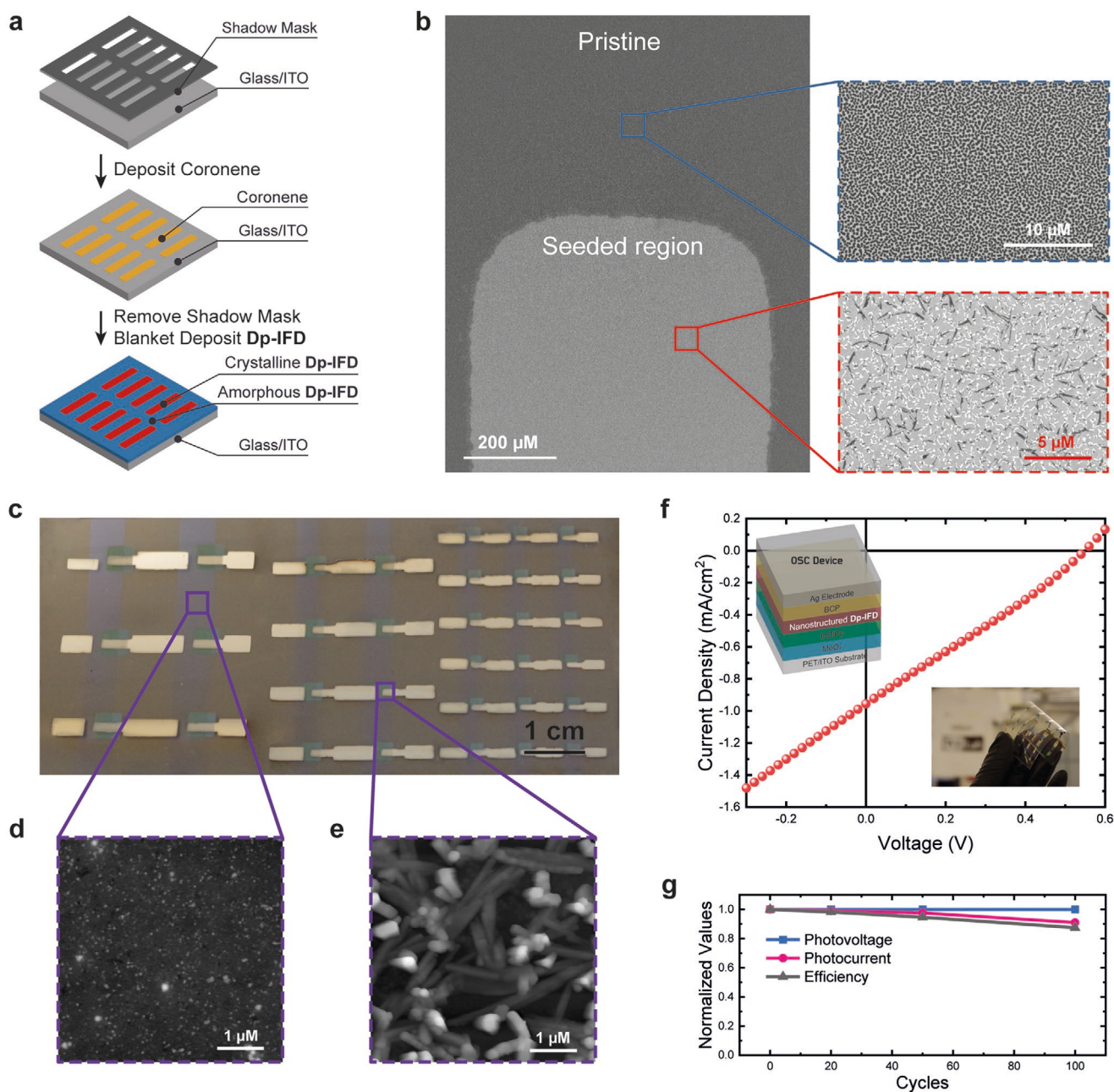


Figure 4. Large-area patterned device arrays. a) Schematic illustration of the procedure to prepare patterned samples. b) SEM images of Dp-IFD film grown on patterned seed-layer on ITO substrate: pristine Dp-IFD film without a seed-layer (upper right) and crystalline Dp-IFD film with a seed-layer (lower right). c) Digital photography of OSC device arrays on PET substrate. d,e) AFM image of PET/ITO surface (d) and the active layer of the device (e). f) Current density-voltage curve of a single device from Figure 4c. g) Photovoltage (blue), photocurrent (red), and efficiency (grey) of the device upon increasing bending cycles at the bending radius of 1 cm.

region. This further corroborates that the ultrathin layer of the coronene seed layer plays a significant role in creating nanostructures through strong intermolecular interactions. This feature is beneficial for the application of large-area patternable devices.

Next, large-area and flexible OSC devices were demonstrated as shown in Figure 4c, with the device architecture of ITO/MoO₃(15 nm)/InClPc(35 nm)/Dp-IFD(40 nm)/BCP(10 nm)/Ag(100 nm). This shows that our seed-induced strategy is readily adaptable to scale-up ultrahigh vacuum deposition process and to create uniform crystalline nanostructures over large areas. While ITO on PET substrate is very smooth (Figure 4d), crystalline nanostructures are observed in the active layer of the device (Figure 4e) due to the seed-induced nanostructuring of Dp-IFD. The device performance under AM1.5 illumination exhibited V_{oc} of 0.55 V, J_{sc} of 1 mA cm⁻², and FF of 0.28, yielding an efficiency of 0.18% (Figure 4f). Notably, the flexible device remains 82% of the photovoltage of the device upon a rigid glass substrate. The lesser photocurrent and FF could be ascribed by the light absorption from the substrate and the recombination at the interface due to the nanostructures. Furthermore, we conducted bending tests at multiple cycles with a bending radius of 1 cm, as shown in Figure 4g. The device was found to keep 88% of its original efficiency after bending for 100 cycles. Meanwhile the V_{oc} and J_{sc} slightly decreased to 99% and 91% of original values, most likely due to the defects in flexible ITO substrate after bending.

3. Conclusion

In conclusion, we developed a novel approach using an ultrathin (<2 nm) nucleation layer of the compound coronene to generate nanostructures of a molecular semiconductor, Dp-IFD, which possesses bulky, free-rotating substituents. The coronene seed layer method for ordering thin films has several advantages, including a low process temperature, the absence of vacuum breaks between steps, and large-area, uniform coverage of nanowires over seeded areas. Transforming Dp-IFD films from disordered to an ensemble of nanowires enables us to unveil several interesting optoelectronic characteristics, such as an increased solid-state luminescence efficiency, concomitant with improved charge transport upon nanostructuring. Dp-IFD nanowires exhibit several orders of magnitude higher SCLC electron mobilities, and four-times stronger solid-state fluorescence quantum yield, as compared to disordered thin films. Notably, the coronene seed layer generates Dp-IFD nanowires when introduced onto any surface, including common glass, silicon or plastic substrates, and any predeposited organic thin films, suggesting that the seed layer can be easily inserted into any point of a pre-existing diode deposition algorithm to realize large-area flexible optoelectronic devices incorporating molecular nanostructures. OLEDs and fullerene-free OSCs containing nanostructured Dp-IFD as an electron-transporting photoactive layer were fabricated using our templating strategy to demonstrate that molecular nanostructures can lead to robust, large-area device arrays on flexible substrates.

4. Experimental Section

Thin Film Fabrication: Si, ITO, and glass substrates were cleaned by sonication with 0.25% aqueous Micro90, deionized water, acetone, and

2-propanol for 10 min each in turn, and dried using compressed N₂ gas. Patterned ITO substrates were used for devices. The substrates were further cleaned using UV-Ozone treatment for 15 min. Dp-IFD, MoO₃, InClPc, coronene, BCP, s-TPD, TPBi, Ag, and Al were purchased from Sigma-Aldrich, Ossila, Lumtec, and Kurt J. Lesker companies and used without further treatment. These materials were fabricated by thermal evaporation at RT using a commercial PVD system (Angstrom Nexdep, USA) under a high vacuum with the base pressure of 5E-7 Torr. The deposition rate was fixed at 0.3 Å s⁻¹, which was monitored by a quartz crystal microbalance during the deposition.

Characterization: Atomic force microscope (AFM, Jupiter XR and Cypher ES, Asylum Research, USA) was utilized for surface topographic images with PPP-NCHR cantilever (NanoSensors, Switzerland). Conductive AFM (c-AFM) measurements were performed using a dual gain ORCA mode with pt/Ir coated PPP-EFM cantilever (NanoSensors, Switzerland). For c-AFM measurements, films were prepared upon ITO substrates, and bias voltage was applied between the tip and the substrate to obtain current values. *I*-*V* curves of thin film samples were recorded over 25 points and averaged.

Surface morphology images were also obtained using field-emission scanning electron microscopy (FE-SEM, Magellan 400, FEI, USA). X-ray diffraction (XRD) of thin-film samples was characterized using SmartLab XRD (Rigaku, Japan). GIWAXS was performed at Soft Matter Interfaces beamline in National Synchrotron Light Source II (NSLS-II, Brookhaven National Laboratory). All samples were placed on a Linkam grazing incident X-ray scattering stage at room temperature inside a vacuum chamber. The photon energy was 16.1 keV with a beam size of 25 μm × 250 μm (height × vertical). All of GIWAXS data were processed using Jupyter Notebook code using Python. In order to obtain absorption spectra of thin-films, the samples were deposited on glass substrates. The spectra were recorded using UV-Vis spectrometer (Evolution 220, Thermo Scientific, USA). Photoluminescence (PL) measurements were carried out using spectrofluorometer (Fluorolog-3, Horiba Scientific), and time-correlated single-photon counting (TCSPC) accessory was utilized for time-resolved PL characterization.

Computation: Density functional theory (DFT) calculations were performed using Gaussian 09 software. Molecular structures were optimized to the ground state using B3LYP functional and a 6-311+G(2d, p) basis set. Excited States calculations were carried out using the time-dependent method under the same functional and basis set. Solvation effect was simulated in solution with chloroform using polarizable continuum model (PCM).

Supporting Information

Supporting Information is available from the Wiley Online Library or from the author.

Acknowledgements

This material was based upon work supported by the National Science Foundation under CBET 1706633. The acquisition of the X-ray diffractometer used in this work was supported by the National Science Foundation Major Research Instrumentation program (CHE-1726578). The authors thank Professor Sankaran Thayumanavan in the Chemistry Department and Professor Stephen S. Nonnenmann in the Mechanical and Industrial Engineering Department at UMass Amherst for graciously granting access to their Jupiter XR and Cypher ES AFMs, respectively.

Conflict of Interest

The authors declare no conflict of interest.

Data Availability Statement

The data that support the findings of this study are available from the corresponding author upon reasonable request.

Keywords

1D nanostructures, flexible electronics, large area optoelectronics, molecular semiconductors, physical vapor deposition

Received: December 21, 2021

Revised: February 4, 2022

Published online: February 24, 2022

- [1] a) Y. Yuan, G. Giri, A. L. Ayzner, A. P. Zoombelt, S. C. Mannsfeld, J. Chen, D. Nordlund, M. F. Toney, J. Huang, Z. Bao, *Nat. Commun.* **2014**, *5*, 3005; b) J. S. Bangsund, T. R. Fielitz, T. J. Steiner, K. Shi, J. R. Van Sambeek, C. P. Clark, R. J. Holmes, *Nat. Mater.* **2019**, *18*, 725; c) H. Cho, S. Lee, N. S. Cho, G. E. Jabbour, J. Kwak, D. H. Hwang, C. Lee, *ACS Appl. Mater. Interfaces* **2013**, *5*, 3855; d) Y. Jiang, Y.-Y. Liu, X. Liu, H. Lin, K. Gao, W.-Y. Lai, W. Huang, *Chem. Soc. Rev.* **2020**, *49*, 5885; e) Y. Jiang, K. F. Li, K. Gao, H. Lin, H. L. Tam, Y. Y. Liu, Y. Shu, K. L. Wong, W. Y. Lai, K. W. Cheah, *Angew. Chem., Int. Ed.* **2021**, *60*, 10007.
- [2] a) B. Wei, J.-Z. Liu, Y. Zhang, J.-H. Zhang, H.-N. Peng, H.-L. Fan, Y.-B. He, X.-C. Gao, *Adv. Funct. Mater.* **2010**, *20*, 2448; b) W. Qin, Z. Yang, Y. Jiang, J. W. Y. Lam, G. Liang, H. S. Kwok, B. Z. Tang, *Chem. Mater.* **2015**, *27*, 3892.
- [3] a) M. A. Fusella, S. Yang, K. Abbasi, H. H. Choi, Z. Yao, V. Podzorov, A. Avishai, B. P. Rand, *Chem. Mater.* **2017**, *29*, 6666; b) B. Du, J. Yi, H. Yan, T. Wang, *Chem.: – Euro. J.* **2021**, *27*, 2908.
- [4] a) E. C. H. Sykes, *Nat. Chem.* **2009**, *1*, 175; b) Z. Li, J. Du, Q. Tang, F. Wang, J.-B. Xu, J. C. Yu, Q. Miao, *Adv. Mater.* **2010**, *22*, 3242; c) X. Hu, Z. Wang, X. Zhu, T. Zhu, X. Zhang, B. Dong, L. Huang, L. Chi, *Small* **2016**, *12*, 4086.
- [5] a) K. Zong, Y. Ma, K. Shayan, J. Ly, E. Renjilian, C. Hu, S. Strauf, A. Briseño, S. S. Lee, *Cryst. Growth Des.* **2019**, *19*, 3461; b) H. Kum, D. Lee, W. Kong, H. Kim, Y. Park, Y. Kim, Y. Baek, S.-H. Bae, K. Lee, J. Kim, *Nat. Electron.* **2019**, *2*, 439.
- [6] Y. Zhang, H. Dong, Q. Tang, S. Ferdous, F. Liu, S. C. Mannsfeld, W. Hu, A. L. Briseno, *J. Am. Chem. Soc.* **2010**, *132*, 11580.
- [7] J. T. Dull, Y. Wang, H. Johnson, K. Shayegan, E. Shapiro, R. D. Priestley, Y. H. Geerts, B. P. Rand, *J. Phys. Chem. C* **2020**, *124*, 27213.
- [8] Y. Hong, J. W. Lam, B. Z. Tang, *Chem. Commun.* **2009**, 4332.
- [9] a) Y. Yoshida, Y. Kumagai, M. Mizuno, K. Isomura, Y. Nakamura, H. Kishida, G. Saito, *Cryst. Growth Des.* **2015**, *15*, 5513; b) Y. Yoshida, K. Isomura, Y. Kumagai, M. Maesato, H. Kishida, M. Mizuno, G. Saito, *J. Phys.: Condens. Matter* **2016**, *28*, 304001.
- [10] a) J. Potticary, L. R. Terry, C. Bell, A. N. Papanikolopoulos, P. C. M. Christianen, H. Engelkamp, A. M. Collins, C. Fontanesi, G. Kociok-Köhn, S. Crampin, E. Da Como, S. R. Hall, *Nat. Commun.* **2016**, *7*, 11555; b) B. Barış, S. Karadeniz, M. O. Erdal, *Mater. Lett.* **2017**, *205*, 70.
- [11] H. Usta, A. Facchetti, T. J. Marks, *Acc. Chem. Res.* **2011**, *44*, 501.
- [12] a) Y. Miyata, T. Minari, T. Nemoto, S. Isoda, K. Komatsu, *Org. Biomol. Chem.* **2007**, *5*, 2592; b) T. Nakagawa, D. Kumaki, J.-i. Nishida, S. Tokito, Y. Yamashita, *Chem. Mater.* **2008**, *20*, 2615; c) Y.-I. Park, J. S. Lee, B. J. Kim, B. Kim, J. Lee, D. H. Kim, S.-Y. Oh, J. H. Cho, J.-W. Park, *Chem. Mater.* **2011**, *23*, 4038; d) C. K. Frederickson, M. M. Haley, *J. Org. Chem.* **2014**, *79*, 11241; e) Z. P. Fan, X. Y. Li, X. E. Luo, X. Fei, B. Sun, L. C. Chen, Z. F. Shi, C. L. Sun, X. Shao, H. L. Zhang, *Adv. Funct. Mater.* **2017**, *27*, 1702318; f) Z.-P. Fan, X.-Y. Li, G. E. Purdum, C.-X. Hu, X. Fei, Z.-F. Shi, C.-L. Sun, X. Shao, Y.-L. Loo, H.-L. Zhang, *Chem. Mater.* **2018**, *30*, 3638.
- [13] K.-W. Park, D. Bilger, T. L. Andrew, *Mol. Syst. Des. Eng.* **2020**, *5*, 110.
- [14] a) M. Nothaft, J. Pflaum, *Phys. Status Solidi B* **2008**, *245*, 788; b) L. Zhang, T. L. Andrew, *Org. Electron.* **2016**, *33*, 135.
- [15] E. Fawcett, J. Trotter, J. M. Robertson, *Proc. R. Soc. London, Ser. A* **1966**, *289*, 366.
- [16] N. Cheng, Y. Peng, T. L. Andrew, *Appl. Phys. Lett.* **2017**, *111*, 133901.
- [17] S. Sharifzadeh, A. Biller, L. Kronik, J. B. Neaton, *Phys. Rev. B* **2012**, *85*, 125307.
- [18] a) J. Mei, N. L. Leung, R. T. Kwok, J. W. Lam, B. Z. Tang, *Chem. Rev.* **2015**, *115*, 11718; b) Z. He, C. Ke, B. Z. Tang, *ACS Omega* **2018**, *3*, 3267.
- [19] Z. Wang, H. Zhang, Z. Wang, B. Zhao, L. Chen, J. Li, H. Wang, Y. Hao, W. Li, *Org. Electron.* **2018**, *57*, 311.
- [20] a) H. Nakanotani, T. Higuchi, T. Furukawa, K. Masui, K. Morimoto, M. Numata, H. Tanaka, Y. Sagara, T. Yasuda, C. Adachi, *Nat. Commun.* **2014**, *5*, 4016; b) X. Chen, Z. Yang, Z. Xie, J. Zhao, Z. Yang, Y. Zhang, M. P. Aldred, Z. Chi, *Mater. Chem. Front.* **2018**, *2*, 1017.
- [21] J. Weickert, R. B. Dunbar, H. C. Hesse, W. Wiedemann, L. Schmidt-Mende, *Adv. Mater.* **2011**, *23*, 1810.